JOURNAL OF GEOPHYSICAL RESEARCH, VOL. 111, D12101, doi:10.1029/2005JD006673, 2006

Observations and simulations of receiver-induced refractivity biases in GPS radio occultation

G. Beyerle,[1] T. Schmidt,[1] J. Wickert,[1] S. Heise,[1] M. Rothacher,[1] G. König-Langlo,[2] and K. B. Lauritsen[3]

Received 15 September 2005; revised 11 January 2006; accepted 1 March 2006; published 16 June 2006.

[1] An analysis of 206,422 atmospheric refractivity profiles observed by the CHAMP georesearch satellite between 14 May 2001 and 30 June 2005 reveals significant biases compared to European Centre for Medium-Range Weather Forecasts meteorological fields at altitudes below 5 km. The mean bias decreases down to −2% at altitudes below 2 km; in the Amazon region, positive biases exceeding +1% are observed. In order to identify bias contributions caused by the receiver signal tracking process an end-to-end simulation study implementing different signal tracking modes was performed. The end-to-end simulations are based on 1992 radiosonde profiles obtained regularly aboard R/V *Polarstern* since December 1982 and were conducted with four receiver models using closed-loop, fly wheeling, and open-loop signal tracking methods. The simulation results confirm that open-loop tracking yields significantly smaller biases and standard deviations of the fractional refractivity errors compared to fly wheeling enabled receivers. In addition, we analyze closed-loop tracking with a second-order loop and demonstrate that similar reductions in biases and standard deviations can be obtained.

Citation: Beyerle, G., T. Schmidt, J. Wickert, S. Heise, M. Rothacher, G. König-Langlo, and K. B. Lauritsen (2006), Observations and simulations of receiver-induced refractivity biases in GPS radio occultation, *J. Geophys. Res.*, *111*, D12101, doi:10.1029/2005JD006673.

1. Introduction

[2] Since February 2001 a Global Positioning System (GPS) radio occultation (RO) experiment aboard the CHAMP (Challenging Minisatellite Payload) georesearch satellite [*Reigber et al.*, 2002, 2005] monitors atmospheric temperature and water vapor with high vertical resolution. The "BlackJack" GPS receiver aboard CHAMP records characteristic signal amplitude and phase changes induced by the ionosphere and neutral atmosphere. From the observed signal phase and amplitude the ray bending angle profile $\alpha(p)$ and subsequently the atmospheric refractivity profile $N(z) = (n(z) - 1) \times 10^6$ are derived. Here, $n(z)$ denotes the real part of the atmospheric refractive index, p and z are the ray impact parameter and the altitude, respectively. For the history and detailed accounts of the radio occultation technique, see, e.g., *Yunck et al.* [2000], *Melbourne et al.* [1994], *Kursinski et al.* [1997], and *Hajj et al.* [2002].

[3] Since activation of the RO experiment aboard CHAMP on 11 February 2001 more than 300,000 occultation events have been observed, 64% of which could be successfully processed and converted to profiles of atmospheric temperature [*Wickert et al.*, 2001, 2004; *Hajj et al.*, 2004]. At altitudes between about 7–8 km and 35 km good agreement between RO measurements and meteorological analyses is found. In the lower troposphere, however, CHAMP validation studies consistently report on a negative refractivity bias of several percent [*Wickert et al.*, 2004; *Marquardt et al.*, 2003; *Ao et al.*, 2003; *Hajj et al.*, 2004]. This negative N bias is well known from the proof-of-concept GPS/MET mission and was first described by *Rocken et al.* [1997] within the GPS/MET data validation study.

[4] The N bias may be attributed to two factors. First, for vertical refractivity gradients below a threshold value of $dN_c/dz \equiv 10^6/r_E \approx -157$ km^{-1} the ray's local radius of curvature falls below r_E, Earth's local radius of curvature. Ray tangent points within the critical layer are inaccessible using a RO geometry with the transmitters located above the layer [*Ao et al.*, 2003; *Sokolovskiy*, 2003, 2004]. In occultation events affected by critical refraction the retrieved bending angles and, subsequently, the retrieved refractivities are systematically smaller than the true values [*Sokolovskiy*, 2004]. Second, the signal tracking process performed by the occultation receiver may induce carrier phase errors which also contribute to the refractivity bias [see e.g., *Gorbunov*, 2002; *Ao et al.*, 2003; *Beyerle et al.*, 2003].

[5] Closed-loop receivers track the incoming GPS carrier signal by correlating it with a model signal generated by a numerically controlled oscillator (NCO) [*Kaplan*, 1996; *Misra and Enge*, 2002]. The NCO's frequency, in turn, is steered toward the incoming signal's frequency with the aid

[1] GeoForschungsZentrum (GFZ), Potsdam, Germany.
[2] Alfred Wegener Institute for Polar and Marine Research, Bremerhaven, Germany.
[3] Danish Meteorological Institute, Copenhagen, Denmark.

0148-0227/06/2005JD006673$09.00

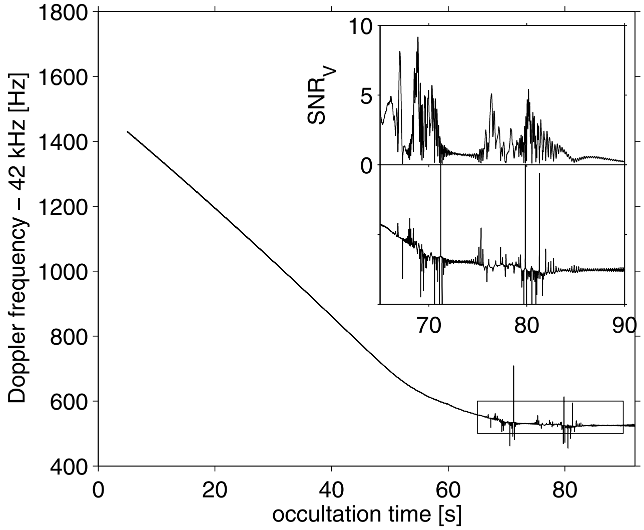

Figure 1. Simulated Doppler frequency profile derived from a radiosonde observation at 29.9°N, 14.6°W on 2 January 1983 (simulation run 10). Insert shows (bottom) the Doppler profile within the multipath zone together with (top) the corresponding voltage signal-to-noise ratio.

of a discriminator that monitors phase deviations between incoming and model signal.

[6] Within regions of multipath ray propagation low signal-to-noise ratios (SNR) are likely to occur causing the discriminator to produce erroneous output values and frequently leading to loss of signal tracking. To solve this problem, the Jet Propulsion Laboratory developed and implemented the fly wheeling tracking technique in the BlackJack occultation receivers aboard CHAMP and SAC-C (Satelite de Aplicaciones Cientificas-C) that is activated once SNR falls below a certain threshold. During fly wheeling the carrier tracking loop is opened and the discriminator values are not extracted from the observed phase deviations but extrapolated on the basis of phase data samples from the previous few seconds [*Hajj et al.*, 2004].

[7] In open-loop signal tracking mode, finally, the receiver NCO is not driven by the observations, but by an a priori Doppler frequency model [*Sokolovskiy*, 2001]. The model is derived from a climatology of atmospheric refractivity possibly including meridional, zonal and/or seasonal variations. Small-scale structures of the true Doppler profile, which are caused by multipath signal propagation, are recorded through changes in the residual phase. It is well established that the implementation of open-loop signal tracking in future RO instruments will prevent the receiver from prematurely losing tracking lock and will provide access to carrier phase and amplitude data in the planetary boundary layer (PBL) even at low latitudes [*Sokolovskiy*, 2001; *Sokolovskiy et al.*, 2005].

[8] Motivated by the improvements expected from the open-loop approach we propose a modification of the currently implemented closed-loop tracking that combines the advantages of both techniques. Figure 1 serves to illustrate our approach. It shows a simulated Doppler profile derived from a tropical radiosonde observation; the sonde data exhibit strong variations in tropospheric humidity. Before about 50 s occultation time, the profile's overall shape is characterized by the smooth relative motion between the transmitter aboard the occulting GPS and the receiver aboard the LEO spacecraft. Later, the impact of the neutral atmosphere delays the signal reducing the magnitude of the mean phase path acceleration from about 3 m s^{-2} to less than 1 m s^{-2}. In this simulated event the Doppler frequency visibly deviates at about 50 s occultation time corresponding to a tangent point altitude of about 28 km. We note, however, that RO observations contain information on atmospheric refractivity at significantly higher altitudes reaching the upper stratosphere [*Kursinski et al.*, 1997]. During the final stage of the occultation, starting at about 67 s occultation time, multipath signal propagation in the midtroposphere and lower troposphere produces interference patterns on the smooth background profile. These phase fluctuations are frequently accompanied by amplitude changes of more than an order of magnitude within a few seconds (Figure 1 insert). The insert shows the Doppler profile within the multipath zone (bottom) together with the corresponding voltage signal-to-noise ratio (top).

[9] Tracking loops of conventional GPS positioning instruments are designed to accommodate arbitrary receiver movements that cause unpredictable phase accelerations; the corresponding voltage signal-to-noise ratio (SNR_v) values, however, are in general considered comparatively stable [*Kaplan*, 1996; *Misra and Enge*, 2002]. Occultation receivers, on the other hand, are exposed to strong SNR_v changes with approximately smooth background Doppler frequencies. The results presented here suggest that in radio occultations it is more important to prevent loss of lock due to low SNR_v and accept larger NCO phase errors than reducing the NCO phase deviations at the risk of losing the signal within regions of low SNR_v.

[10] The outline of the paper is as follows. In section 2 the two observational data sets, a database of radiosonde observations collected aboard R/V *Polarstern* and archived by Alfred Wegener Institute for Polar and Marine Research (AWI) as well as the CHAMP satellite observations are briefly described. Section 3 discusses the end-to-end simulation chain emphasizing the signal tracking models. In section 4, biases of CHAMP refractivity profiles with respect to meteorological analyses are described and discussed. We restrict the comparisons to atmospheric refractivity; for discussions of temperature and water vapor retrievals, see, e.g., *Healy* [2001], *Marquardt et al.* [2001], *Kursinski and Hajj* [2001], and *Heise et al.* [2006]. Furthermore, the simulation results using closed-loop and open-loop signal tracking schemes are analyzed. Section 5 comments on the feasibility of data wipe off to permit the implementation of four-quadrant carrier phase extraction, and section 6 summarizes the main conclusions.

2. Observational Data Sets

2.1. *Polarstern* Radiosonde Data

[11] Starting in December 1982 the AWI radiosonde data set comprises almost 25,000 profiles observed aboard R/V *Polarstern* at latitudes between 78.2°S and 89.9°N. Balloon-borne sondes measure temperature, pressure and humidity data with a vertical resolution of about 20–50 m (corresponding to 5–10 s sampling time at 4–5 m s^{-1}

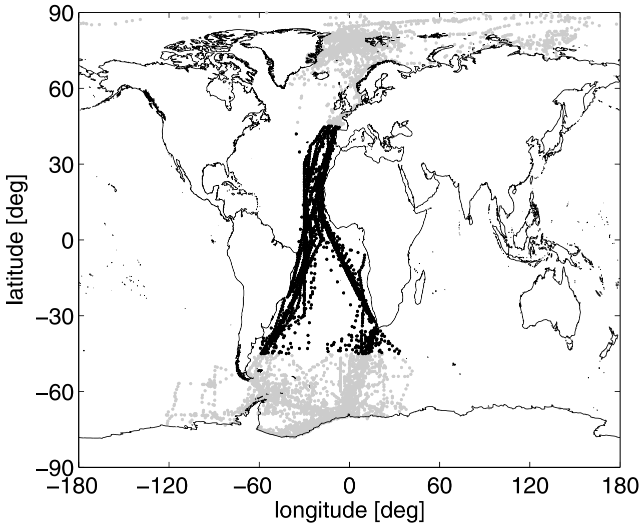

Figure 2. Map of aerological soundings performed aboard research vessel *Polarstern* between December 1982 and June 2005 (grey and black dots). The present analysis is focused on 1992 sonde observations recorded between 45°S and 45°N (black dots).

balloon rise velocity). Sounding aboard *Polarstern* is performed with Vaisala RS80 radiosondes [*Vaisala*, 1989]. The manufacturer quotes the following repeatabilities of calibration: 0.2–0.4°C temperature accuracy between −90°C and +60°C, 0.5 hPa pressure accuracy between 1060 hPa and 3 hPa and 2% RH relative humidity accuracy between 0 and 100% RH. At low temperatures it is known that the accuracy of the humidity measurements decreases further [see, e.g., *Leiterer et al.*, 1997].

[12] With very few exceptions critical refraction in the lower troposphere is caused by strong vertical gradients induced by the water vapor field [*von Engeln et al.*, 2003; A. von Engeln et al., The impact of thin water vapor layers on CHAMP radio occultation measurements, submitted to *Radio Science*, 2005]; humidity values at high latitudes are in general too low to produce critical refraction layers. Thus we focus in the following on the subset of 1992 sonde profiles recorded at midlatitudes and low latitudes ranging from 45°S to 45°N. The corresponding launch dates cover the time period between 29 December 1982 and 16 June 2005. Figure 2 shows the geographical locations of the corresponding sonde launches.

[13] Refractivity N is calculated from observed pressure p, water vapor partial pressure p_w and temperature T from [*Bevis et al.*, 1994]

$$N = k_1 \frac{p - p_w}{T} + k_2 \frac{p_w}{T} + k_3 \frac{p_w}{T^2} \qquad (1)$$

with $k_1 = 0.7760$ K Pa^{-1}, $k_2 = 0.704$ K Pa^{-1}, and $k_3 = 3.739 \times 10^3$ K^2 Pa^{-1}. Above the balloon burst height z_B the refractivity profiles are extrapolated using

$$N(z) = N(z_B) \exp\left(-\frac{z - z_B}{H}\right) \qquad z > z_B \qquad (2)$$

where $H = 7$ km denotes the scale height.

2.2. CHAMP Satellite Observations

[14] As of 30 June 2005 (day of year 181), 320,904 occultation events have been recorded aboard CHAMP since activation of the operational occultation mode on 14 May 2001 (day of year 134). Out of these, 206,422 observations (64.3%) pass the quality criteria imposed by the operational processing system and produce validated refractivity profiles (level 3 data). The current version of the GFZ's occultation processing system (version 5) uses double differencing to retrieve excess phase paths [*Wickert et al.*, 2001, 2004] and the full spectrum inversion (FSI) method [*Jensen et al.*, 2003] to obtain bending angles at tropospheric altitudes. The bending angle profiles are truncated at that impact parameter value where the smoothed FSI amplitude drops to 50% of the maximum value. For a detailed discussion of the data processing and analysis, see *Wickert et al.* [2001, 2004].

[15] The observed CHAMP refractivity profiles are intercompared with meteorological analysis results provided by the European Centre for Medium-Range Weather Forecasts (ECMWF). ECMWF pressure and temperature values are calculated by linear interpolation between grid points (0.5° × 0.5° resolution). Linear interpolation in time is performed between 6 h ECMWF analyses fields. The vertical resolution of the observed RO refractivity profiles is 200 m [*Wickert et al.*, 2004]; the comparison between observation and ECMWF, however, is performed on the 60 levels provided by the ECMWF atmospheric model ranging from the ground surface up to about 60 km altitude. Geopotential height at each level is calculated from the analysis fields using the hydrostatic equation and converted to geometric height (M. J. Mahoney, A discussion of various measures of altitude, available at http://mtp.jpl.nasa.gov/notes/altitude/altitude.html). Within the altitude range relevant for this study vertical spacing of the model grid points are of the same order as the observations increasing from about 200 m at 1 km altitude to about 700 m at 10 km altitude. (For a discussion of possible aliasing effects, however, see *Kursinski et al.* [2000] and *Kuo et al.* [2004].)

[16] Negative biases in the lower troposphere are well known from CHAMP and other satellite RO missions [see, e.g., *Rocken et al.*, 1997; *Ao et al.*, 2003; *Hajj et al.*, 2004]. The exact shape of the fractional refractivity error, however, depends on the number of data points retrieved at a given altitude z, in the following denoted by $m(z)$; the loss-of-lock altitude $z_{50\%}$ refers to the altitude at which the number of successfully retrieved data points is reduced to 50%. If, e.g., more restrictive quality control criteria are employed removing outlier observations, $z_{50\%}$ increases correspondingly. If the fraction is above 50% within the full altitude range, $z_{50\%}$ is undefined. A plot of $m(z)$ is attached to all figures showing the fractional refractivity error $\Delta N/N_{\text{true}} \equiv (N - N_{\text{true}})/N_{\text{true}}$ in order to emphasize the mutual dependence between fractional refractivity error and $m(z)$.

3. End-to-End Simulations

[17] Starting from a refractivity profile $N(z)$, the atmospheric propagation of a GPS signal is modeled using the inverse FSI technique [*Gorbunov*, 2003; *Gorbunov and Lauritsen*, 2004]. With the FSI method the simulated amplitude and phase data are converted to bending angle

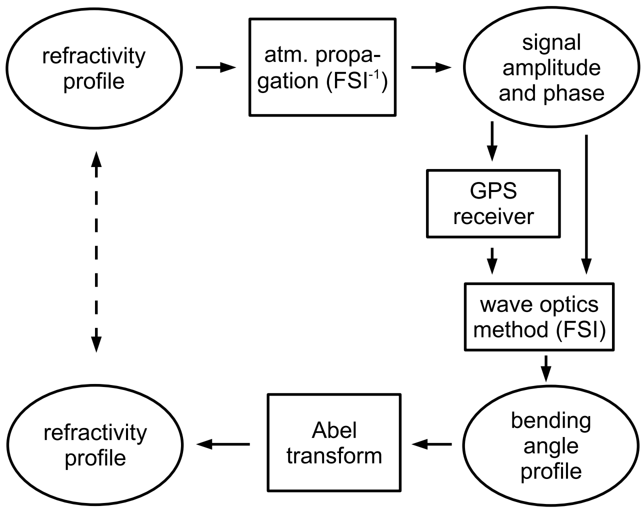

Figure 3. Schematic overview of the end-to-end simulation procedure. Using the inverse FSI method, the atmospheric propagation of a GPS signal based on a refractivity profile is modeled. The signal is converted to a bending angle profile; its Abel transformation yields the retrieved refractivity profile closing the simulation loop. Optionally, a GPS receiver model is inserted into the simulation chain.

profiles [*Jensen et al.*, 2003]. Finally, refractivity profiles are retrieved by Abel transforming the bending angle profiles thereby closing the simulation loop [*Ao et al.*, 2003]. Optionally, a simplified signal receiver model can be inserted in the end-to-end simulation chain. Its schematic is shown in Figure 3. For each receiver model and three noise levels 1992 simulation runs are performed using spherically symmetric refractivity fields derived from the *Polarstern* radiosonde profiles as described in section 2.1.

[18] For numerical efficiency the simulations are simplified in a number of ways:

[19] 1. The GPS and LEO orbits are assumed to be coplanar and circular with radii of r_G = 26,800 km and r_L = 6800 km, respectively. Thus FSI and inverse FSI are efficiently implemented using the Fast Fourier Transform without the requirement of vacuum propagation of the wavefield or the addition of phase correction terms [*Jensen et al.*, 2003; *Gorbunov*, 2003; *Gorbunov and Lauritsen*, 2004].

[20] 2. Since the optical path difference between interfering rays in multipath regions are much smaller than the coarse acquisition code's (C/A code) chip length of 300 m [*Kaplan*, 1996; *Misra and Enge*, 2002], code modulation is not taken into account [*Beyerle et al.*, 2003]. The simulated signal is modulated with the 50 Hz navigation data, though, since the data modulation is relevant for the selected method of carrier phase extraction (see section 3.2.1).

[21] 3. Relativistic Doppler shifts and clock deviations are not included in the simulation. For a detailed discussion, see *Ashby* [2003].

[22] 4. The carrier tracking loops update only the NCO frequency, phase update loops are not considered [*Stephens and Thomas*, 1995].

[23] 5. Since the simulations are focused on altitudes below 10 km, signal propagation through the ionosphere is not taken into account. In real RO events the ionosphere induces carrier phase path deviations on the order of several tens of meters which have to be corrected for by simultaneous observations at both GPS frequencies, L1 and L2 [see, e.g., *Syndergaard*, 2000]. In this study, however, dispersion is ignored and only L1 data are generated.

3.1. Forward Propagation

[24] The optical path length differences between interfering rays in multipath regions are much smaller than the C/A code chip (and navigation bit) lengths, as already indicated [*Beyerle et al.*, 2003]. In order to efficiently simulate the propagation process from the transmitter to the receiver the signal is modeled as modulation-free, i.e., a pure tone. Atmospheric propagation of GPS signals is implemented using the inverse FSI technique [*Gorbunov*, 2003; *Gorbunov and Lauritsen*, 2004]. First, the bending angle profile $\alpha(p)$ as a function of impact parameter p is determined from the observed refractive index profile $n(p)$ using the inverse Abel transform [*Fjeldbo et al.*, 1971]:

$$\alpha(p) = -2p \int_p^\infty \frac{dx}{\sqrt{x^2 - p^2}} \frac{d\ln(n(x))}{dx} \tag{3}$$

where the integral's upper limit is approximated as r_E + 150 km. From $\alpha(p)$ the signal amplitude $A(t)$ and phase $\Phi(t)$ at the LEO's location is calculated with the inverse FSI method [*Gorbunov*, 2003; *Gorbunov and Lauritsen*, 2004]. Random sign changes every 20 ms simulate the 50 Hz data modulation of the signal $u(t)$, i.e.,

$$u(t) \equiv D(t)\, A(t)\, \cos(\Phi(t) - \Phi_0) \tag{4}$$

with data modulation $D(t) = \pm 1$ [*Ao et al.*, 2003] and $\Phi_0 \equiv \Phi(t = 0)$. $D(t)$ is taken to be piecewise constant over periods of 20 ms.

3.2. Receiver Models

[25] The receiver tracks the signal $u(t)$ by correlating $u(t)$ with replica signals $v^i(t) \equiv \cos[\Phi^{\mathrm{NCO}}(t)]$ and $v^q(t) \equiv -\sin[\Phi^{\mathrm{NCO}}(t)]$. The replicas $v^i(t)$ and $v^q(t)$ are generated by the receiver's NCO [*Kaplan*, 1996; *Tsui*, 2000; *Misra and Enge*, 2002]. In our simulation the NCO's frequency $f^{\mathrm{NCO}}(t)$ is updated at a rate of $1/T$ = 1 kHz, i.e., $f^{\mathrm{NCO}}(t)$ is piecewise constant for $t_n \le t < t_n + T$, $f_n^{\mathrm{NCO}} \equiv f^{\mathrm{NCO}}(t_n)$. Provided the amplitude $A(t)$ and frequency $f(t) \equiv 1/(2\pi)d\Phi/dt$ can be approximated as piecewise constant functions, $A_n \equiv A(t_n)$ and $f_n \equiv f(t_n)$, the inphase and quadphase correlation sums are given by

$$\begin{aligned} i_n &\equiv \frac{2}{T}\int_{t_n}^{t_n+T} u(t)\, v^i(t)\, dt + N_n^i \\ &\approx D_n A_n \,\mathrm{sinc}(\pi\, \Delta f_n\, T) \cos(\pi\, \Delta f_n\, T + \Delta\Phi_n) + N_n^i \\ &= D_n A_n \,\mathrm{sinc}(\pi\, \Delta f_n\, T) \cos\left(\frac{\Delta\Phi_n + \Delta\Phi_{n+1}}{2}\right) + N_n^i \end{aligned} \tag{5}$$

and

$$
\begin{aligned}
q_n &\equiv \frac{2}{T}\int_{t_n}^{t_n+T} u(t)\, v^q(t)\, dt + N_n^q \\
&\approx D_n A_n \mathrm{sinc}(\pi\, \Delta f_n\, T)\sin(\pi\, \Delta f_n\, T + \Delta\Phi_n) + N_n^q \\
&= D_n A_n\, \mathrm{sinc}(\pi\, \Delta f_n\, T)\sin\left(\frac{\Delta\Phi_n + \Delta\Phi_{n+1}}{2}\right) + N_n^q \qquad (6)
\end{aligned}
$$

respectively, with $\mathrm{sinc}(x) \equiv \sin(x)/x$ and $D_n \equiv D(t_n)$. Here, $\Delta f_n \equiv f_n - f_n^{\mathrm{NCO}}$ and $\Delta\Phi_n \equiv \Phi_n - \Phi_n^{\mathrm{NCO}}$ denote the difference between the true frequency f_n and the NCO frequency f_n^{NCO} and the difference between the true phase Φ_n and the NCO phase Φ_n^{NCO}, respectively. Here and in the following the subscript n denotes the corresponding function value at time t_n, i.e., $f_n \equiv f(t_n)$ and $\Phi_n \equiv \Phi(t_n)$, except where noted otherwise. The NCO and true phases follow from

$$
\begin{aligned}
\Phi_n^{\mathrm{NCO}} &\equiv 2\pi\, T \sum_{j=1}^{n-1} f_j^{\mathrm{NCO}} \\
\Phi_n &\equiv 2\pi\, T \sum_{j=1}^{n-1} f_j
\end{aligned}
\qquad (7)
$$

We note that Φ_n^{NCO} and Φ_n are accumulated phases and not restricted to the interval $[-\pi, +\pi]$. Gaussian white noise, N_n^i and N_n^q, with zero mean and standard deviations

$$\sigma\left(N_n^{i,q}\right) = \frac{A^{(0)}}{\sqrt{2\, T\, 10^{\mathrm{C/N_0}/10}}} \qquad (8)$$

is added to the correlation sums, i_n and q_n (equations (5) and (6)), where $A^{(0)}$ denotes the amplitude for vacuum propagation and $\mathrm{C/N_0}$ is the carrier-to-noise density ratio expressed in dB Hz [*Kaplan*, 1996].

[26] The total accumulated phase is the sum of NCO phase Φ_n^{NCO} and residual phase Φ_n^R (see section 3.2.1):

$$\varphi_n^{\mathrm{Rcv}} \equiv \Phi_n^{\mathrm{NCO}} + \Phi_n^R \qquad (9)$$

Finally, output data volume is compressed from $1/T = 1$ kHz to 50 Hz by coherent summation over $K = 20$ samples

$$
\begin{aligned}
I_k &= \sum_{j=K(k-1)+1}^{Kk} i_j \\
Q_k &= \sum_{j=K(k-1)+1}^{Kk} q_j \\
\Phi_k^{\mathrm{Rcv}} &= \frac{1}{K}\sum_{j=K(k-1)+1}^{Kk} \varphi_j^{\mathrm{Rcv}}
\end{aligned}
\qquad (10)
$$

In the following, I_k and Q_k are denoted as coherent inphase and quadphase correlation sums, respectively. We note that according to equation (10), Φ_k^{Rcv} is taken to be the mean value of φ_j^{Rcv}, *Thomas* [1989] discusses more sophisticated alternatives. From the coherent correlation sums the signal amplitudes

$$A_k^{\mathrm{Rcv}} = \sqrt{(I_k)^2 + (Q_k)^2} \qquad (11)$$

are obtained. Signal tracking is accomplished in either closed-loop or open-loop mode. The two modes will be discussed in sections 3.2.2 and 3.2.3.

3.2.1. Residual Phase Extraction

[27] The residual phases Φ_n^R (equation (9)) are extracted from the correlation sums (equations (5) and (6)) using two different methods. Within the two-quadrant phase extraction scheme the residual phases are

$$\Phi_{n+1}^R = \mathrm{atan}\left(\frac{q_n}{i_n}\right) \qquad (12)$$

Provided $|i_n| \gg |N_n^i|$ and $|q_n| \gg |N_n^q|$ (equations (5) and (6)), equation (12) may be approximated by

$$\Phi_{n+1}^R \approx \mathrm{atan}\left(\tan\left(\frac{\Delta\Phi_n + \Delta\Phi_{n+1}}{2}\right)\right) \qquad (13)$$

Two-quadrant phase extraction is commonly used in GPS receivers since Φ_{n+1}^R, as derived from equation (13), does not dependent on the data modulation values D_n [*Kaplan*, 1996]. On the other hand, the validity of equation (12) (and (13)) is restricted to the phase interval $[-\pi/2, +\pi/2]$. If the phase deviations exceed $\pm\pi/2$ an erroneous offset of $\pm\pi$ between derived residual phase and true phase error is introduced since $\mathrm{atan}(\tan(x)) = x$ only if $-\pi/2 \le x \le \pi/2$, but $\mathrm{atan}(\tan(x)) = x \pm \pi$ otherwise.

[28] To obtain valid residual phases for phase deviations larger than $+\pi/2$ and smaller than $-\pi/2$, the following four-quadrant phase extraction scheme is used

$$\Phi_{n+1}^R = \mathrm{atan2}\left(\frac{q_n}{D_n}, \frac{i_n}{D_n}\right) \qquad (14)$$

Four-quadrant phase extraction according to equation (14), though, presupposes knowledge of the data modulation D_n.

[29] In closed-loop mode the phase-locked loop (PLL) steers the residual phase Φ_{n+1}^R toward zero, i.e., $|i_n| \gg |q_n|$ if the tracking loop is locked to the signal. In open-loop mode (section 3.2.3), however, received and replica signals are no longer phase locked, Φ_{n+1}^R possibly exceeds the interval $[-\pi, +\pi]$ and use of equation (14) would introduce a cycle slip whenever Φ_{n+1}^R passes $\pm\pi$. These cycle slips are eliminated by adding the number of full cycles to Φ_{n+1}^R, i.e., equation (14) is modified by

$$\Phi_{n+1}^R = \mathrm{atan2}\left(\frac{q_n}{D_n}, \frac{i_n}{D_n}\right) + C_n \qquad (15)$$

where

$$C_n = \begin{cases} C_{n-1} - 2\pi & : \quad \mathrm{atan2}\left(\frac{q_n}{D_n}, \frac{i_n}{D_n}\right) - \mathrm{atan2}\left(\frac{q_{n-1}}{D_{n-1}}, \frac{i_{n-1}}{D_{n-1}}\right) < -\pi \\ C_{n-1} + 2\pi & : \quad \mathrm{atan2}\left(\frac{q_n}{D_n}, \frac{i_n}{D_n}\right) - \mathrm{atan2}\left(\frac{q_{n-1}}{D_{n-1}}, \frac{i_{n-1}}{D_{n-1}}\right) > +\pi \\ C_{n-1} & : \quad \text{else} \end{cases} \tag{16}$$

and $C_1 = 0$.

[30] In the current CHAMP occultation, receiver closed-loop tracking with two-quadrant phase extraction is implemented [*Ao et al.*, 2003]. Four-quadrant phase extraction, on the other hand, records the data modulation bits and introduces half cycles whenever a bit transition occurs. Thus four-quadrant phase extraction presupposes the removal of the 50 Hz data modulation prior to signal correlation (data demodulation or data wipe off) and necessitates knowledge of the navigation message. We comment on the feasibility of data wipe off in section 5.

3.2.2. Closed-Loop Tracking

[31] To study the sensitivity of retrieved refractivities with respect to the chosen tracking loop parameters, the simulation receiver's carrier loop bandwidths are varied between 5 and 30 Hz and loops of order two and three are implemented. In closed-loop mode the NCO frequency is adjusted every C/A code period (about 1 ms) by $\delta f_{n+1}^{\mathrm{NCO}} \equiv f_{n+1}^{\mathrm{NCO}} - f_n^{\mathrm{NCO}}$. The frequency adjustment for the time interval $[t_{n+1}, t_{n+2}]$ is

$$\delta f_{n+1}^{\mathrm{NCO}} = \frac{1}{T}\left(\frac{K_1^{(2)} + K_2^{(2)}}{2\pi}\,\Phi_{n+1}^R + \frac{-K_1^{(2)}}{2\pi}\,\Phi_n^R\right) \tag{17}$$

(second-order loop) or

$$\delta f_{n+1}^{\mathrm{NCO}} = \delta f_n^{\mathrm{NCO}} + \frac{1}{T}\left(\frac{K_1^{(3)} + K_2^{(3)} + K_3^{(3)}}{2\pi}\,\Phi_{n+1}^R + \frac{-2\,K_1^{(3)} - K_2^{(3)}}{2\pi}\,\Phi_n^R + \frac{K_1^{(3)}}{2\pi}\,\Phi_{n-1}^R\right) \tag{18}$$

(third-order loop), respectively, where the residual phase Φ_n^R is given in radian and $K_1^{(2)} = 7.358 \times 10^{-2}$, $K_2^{(2)} = 2.810 \times 10^{-3}$ for a standard-underdamped second-order loop and $K_1^{(3)} = 7.172 \times 10^{-2}$, $K_2^{(3)} = 2.383 \times 10^{-3}$, $K_3^{(3)} = 3.020 \times 10^{-5}$ for a standard-underdamped third-order loop [*Stephens and Thomas*, 1995]. In both cases, tracking loop bandwidth is taken to be 30 Hz. For comparison, simulation runs with loop bandwidth reduced to 5 Hz are performed as well; 5 Hz was chosen since it is the smallest bandwidth value given by *Stephens and Thomas* [1995]. The corresponding third-order loop parameters are $K_1^{(3)} = 1.283 \times 10^{-2}$, $K_2^{(3)} = 7.365 \times 10^{-5}$ and $K_3^{(3)} = 1.590 \times 10^{-7}$. With $\delta f_{n+1}^{\mathrm{NCO}}$ the NCO frequency of the $(n + 1)$th update interval follows from $f_{n+1}^{\mathrm{NCO}} = \delta f_{n+1}^{\mathrm{NCO}} + f_n^{\mathrm{NCO}}$ and subsequently i_{n+1} and q_{n+1} are calculated using equations (7), (5), and (6).

3.2.3. Open-Loop Tracking

[32] Open-loop tracking is commonly considered a possible solution to the problem of premature loss of lock in closed-loop receivers [*Sokolovskiy*, 2001]. In open-loop mode the loop feedback $\delta f_{n+1}^{\mathrm{NCO}}$ is calculated from a Doppler frequency model $f^{\mathrm{model}}(t_n) \equiv f_n^{\mathrm{model}}$, i.e.,

$$f_{n+1}^{\mathrm{NCO}} = f_{n+1}^{\mathrm{model}} \tag{19}$$

and therefore

$$\delta f_{n+1}^{\mathrm{NCO}} = f_{n+1}^{\mathrm{model}} - f_n^{\mathrm{NCO}} \tag{20}$$

For simplicity, in this study the model f_n^{model} is taken to be the ensemble average

$$f_n^{\mathrm{model}} \equiv \frac{1}{N_R}\sum_{j=1}^{N_R} f_n^{(j)} \equiv \left\langle f_n^{(j)} \right\rangle \tag{21}$$

where N_R = 1992 and $f_n^{(j)}$ is the true signal frequency derived from the jth simulated Doppler profile at time interval n. The one-sigma standard deviation is about 10–20 Hz in good agreement with *Sokolovskiy* [2001]. Total phase is calculated from equation (9), with Φ_n^R extracted from equation (15) and Φ_n^{NCO} is derived from the NCO frequency (equation (7)). Analogous to the closed-loop case the sampling rate is reduced from 1 kHz to 50 Hz using equation (10), and equation (11) yields the signal amplitude. Thus, in open-loop mode the total phase is not a raw data product provided by the receiver, but instead is calculated in postprocessing from the inphase and quadphase correlation sums taking into account the (known) 50 Hz navigation data.

3.2.4. Fly Wheeling Mode Tracking

[33] The first occultation measurements from the proof-of-concept GPS/MET mission frequently suffered from loss of lock already in the upper or midtroposphere in particular at low latitudes [*Rocken et al.*, 1997]. To solve this problem, the Jet Propulsion Laboratory developed and implemented the fly wheeling tracking method [*Hajj et al.*, 2004]. The fly wheeling mode was successfully used in later phases of the GPS/MET mission and is the nominal tracking mode on the CHAMP and SAC-C satellites.

[34] Fly wheeling tracking is activated when $\mathrm{SNR_v}$ drops below a predefined threshold value $\mathrm{SNR_v^*}$. Once activated, the tracking loop is opened and f_{n+1}^{NCO} is calculated from the previous L NCO frequencies by extrapolating a polynomial fit through $f_{n-L+1}^{\mathrm{NCO}}, \ldots, f_n^{\mathrm{NCO}}$. Thus, during fly wheeling the carrier tracking loop is no longer phase locked to the signal $u(t)$. The phasor $I + iQ$ starts to rotate freely in $I - Q$ space, effectively randomizing the residual phase values and thereby enhancing the occurrence probability of carrier phase cycle slips. However, signal loss is less likely during fly wheeling since large residual phase errors no longer cause f_n^{NCO} to sheer out.

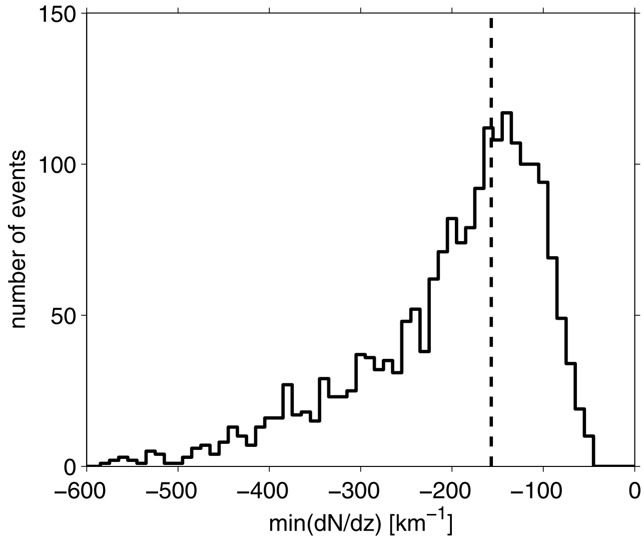

Figure 4. Histogram distribution of the minimum of the vertical refractivity gradient, $dN(z)/dz$. The dashed line marks the threshold value for critical refraction $dN_c(z)/dz = -157\ \mathrm{km}^{-1}$.

[35] Our fly wheeling simulations show that the results depend strongly on the selected fly wheeling parameters: the number of samples L included in the polynomial fit, the degree of the extrapolation polynomial, the amplitude thresholds for activation and deactivation, possible time delays, etc. In our implementation the following parameters were found to give best results: $L = 2000$ corresponding to a time period of 2 s, a linear fit and a threshold value of $\mathrm{SNR}_V^* = 40$ V/V. If the observed amplitude falls below SNR_V^* for more than 100 ms, fly wheeling is activated for at least 2 s. We stress that the design choices of our fly wheeling implementation were made to achieve consistency with the CHAMP occultation data; the implementation should not be regarded as an accurate model of the BlackJack receiver aboard CHAMP.

3.3. Backward Model

[36] From the amplitudes A_k^{Rcv} and phases Φ_k^{Rcv} (equation (10)) bending angle profiles are derived with the FSI technique [*Jensen et al.*, 2003; *Gorbunov and Lauritsen*, 2004]. The bending angle profiles are inverted to refractivity profiles using the Abel transform [*Fjeldbo et al.*, 1971] thereby closing the simulation chain.

4. Analysis and Discussion

4.1. Sonde and Satellite Observations

[37] From the *Polarstern* in situ measurements all soundings located between 45°S and 45°N latitude are selected and the refractivity profiles $N(z)$ are calculated. Eighty-four out of 2076 soundings are removed from the data set since they contain discontinuities in the relative humidity values exceeding 50% RH or consist of less than 10 measurement samples. The remaining 1992 profiles are linearly interpolated on an altitude grid with 5 m resolution and low-pass filtered using a running mean with 150 m width to reduce measurement noise introduced by the humidity sensor [*Vaisala*, 1989]. We ignore the sonde's horizontal motion during ascent (or, equivalently, we assume spherical symmetry of the refractivity field) and identify the changes of $N(z)$ with the vertical refractivity gradient dN/dz. The occurrence distribution of the smallest value of dN/dz is shown in Figure 4; 58.3% (1162 profiles) exhibit critical refraction with $dN/dz < -157\ \mathrm{km}^{-1}$ (dashed line). These percentage estimates, however, should be regarded as an upper limit for the occurrence of critical refraction in the marine environment at low and midlatitudes, since radiosonde data represent point measurements without information on the horizontal extent of the observed layers [see, e.g., *von Engeln et al.*, 2003]. The probability for the occurrence of critical refraction as a function of altitude can be inferred from Figure 5 which shows the altitude distribution of the highest layer obeying $dN/dz < -157\ \mathrm{km}^{-1}$. Figure 5 suggests that critical refraction is a phenomenon restricted to the PBL at altitudes below 2–2.5 km. Above 3 km, critical layers are unlikely to occur [see also *Gorbunov et al.*, 1996].

[38] The CHAMP refractivity bias derived from 11,626 observations over the Atlantic Ocean between 45°S–0°S, 45°W–15°E and 0°N–45°N, 45°W–15°W is plotted in Figure 6 (solid lines). While the N bias is below 0.2% in the midtroposphere at altitude between 5 and 13 km, it decreases to −3% within the PBL. The occurrence distribution shown in Figure 5 suggests that critical refraction contributes to the observed deviation only below 3 km. The smaller negative bias between 3 and 5 km altitude, however, most likely is caused by the receiver tracking as discussed in section 4.2.

[39] The large volume of the CHAMP occultation data set allows for a N bias analysis not only in terms of zonal and/or meridional averages but also as a function of longitude and latitude. 206,422 profiles of the fractional refractivity deviation between CHAMP and ECMWF are sorted in $10° \times 10°$ longitude/latitude bins. Within each bin the mean value between 3 and 5 km altitude is computed and plotted

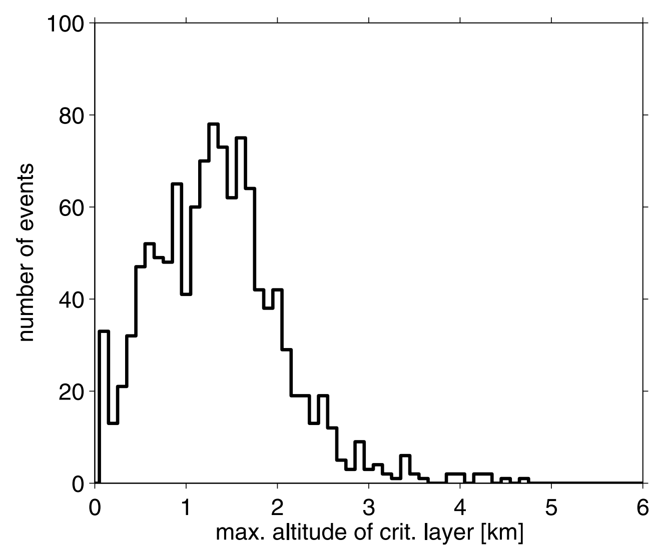

Figure 5. Histogram distribution of the highest altitude at which refractivity gradients below the critical threshold value are found.

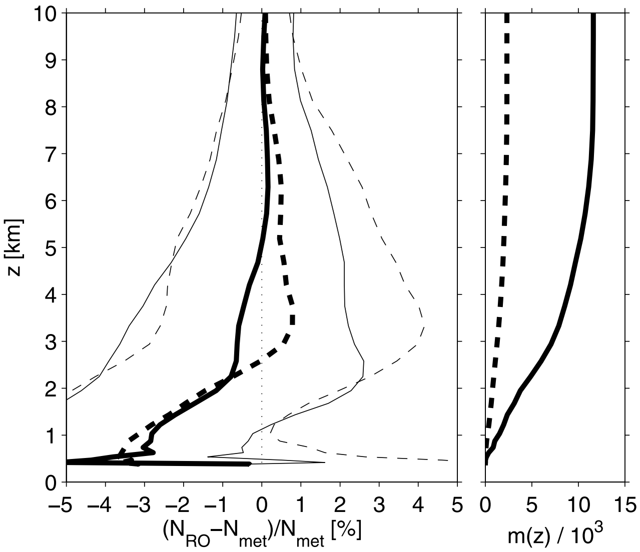

Figure 6. (left) Fractional refractivity deviation between CHAMP refractivity N_{RO} and ECMWF analyses N_{met} restricted to a subset of 11,626 observations over the Atlantic (solid line). The dashed line marks the corresponding result derived from 2336 occultation events over the Amazon region. The corresponding one-sigma standard deviations are plotted as thin lines. (right) Number of observed refractivity data as a function of altitude. The loss-of-lock altitudes are $z_{50\%}$ = 2.5 (Atlantic) and 2.8 km (Amazon region), respectively.

in Figure 7. On average, there are 306 ± 101 observations per bin.

[40] At high latitudes the fractional refractivity error remains below ±0.3%, at midlatitudes and low latitudes the bias reaches below −1% on a global scale. The geographical distribution, however, exhibits pronounced patterns with small and medium-scale biases exceeding +1% over South America and −2% over the eastern tropical Pacific. The simulation results discussed below suggest that the negative bias is consistently explained by receiver-induced tracking errors (within the altitude range of 3–5 km the occurrence of critical refraction is not expected). The explanation for the positive biases over the Amazon region and Indonesia requires a detailed analysis which is beyond the scope of this study. One of the possibilities that should be investigated is the occurrence of positive vertical refractivity gradients (refractivity increases with altitude) leading to subrefraction; *Sokolovskiy* [2004] discusses an individual sonde profile that exhibits subrefraction and yields a positive refractivity bias. The solid white lines mark the geographical region of observations plotted as solid lines in Figure 6, and the Amazon data are plotted as dashed lines. Figure 6 demonstrates the positive bias of this subset and its enhanced standard deviation (thin dashed lines). The corresponding 50% altitudes are 2.5 km (Atlantic) and 2.8 km (Amazon region), respectively.

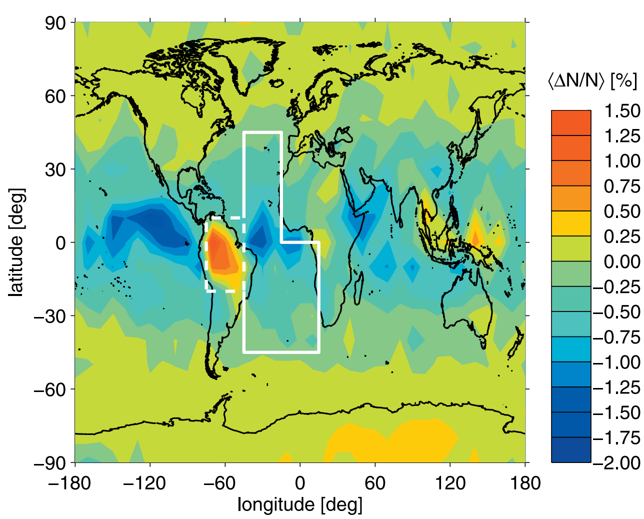

Figure 7. Global map of fractional refractivity deviation between CHAMP observations and corresponding ECMWF analyses. The mean deviations between 3 and 5 km altitude are calculated from 206,422 profiles sorted into 10° × 10° longitude/latitude bins. White lines mark the regions of the two subsets plotted in Figure 6.

4.2. End-to-End Simulations

[41] The task of interpreting the N bias below 5 km (Figure 6) is approached by a series of end-to-end simulation runs; the results are presented in Figures 8–13. Figures 8 (left) to 13 (left) show the mean fractional difference between retrieved and true refractivity (thick lines). Thin lines mark the one-sigma standard deviation. In addition, the number of retrieved data points as function of altitude is indicated as well (Figures 8, right, to 13, right).

[42] The simulations are performed for signal-to-noise density ratios of 40, 45 and 50 dB Hz. This choice is

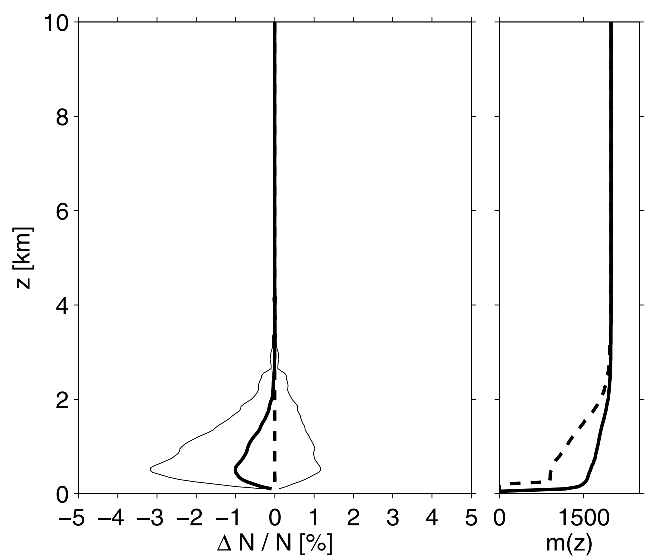

Figure 8. (left) Fractional refractivity error derived from simulations using the ideal receiver (model A) is plotted as thick solid line. The thin lines indicate the one-sigma standard deviation. Excluding data affected by critical refraction yield an almost bias-free result (dashed lines) with a standard deviation of less than 0.03%. (right) Number of retrieved data points. $z_{50\%}$ are 692 m and 99.5 m, respectively.

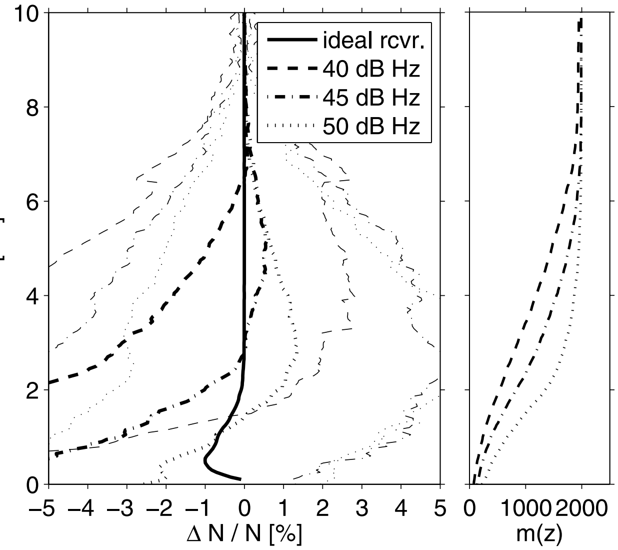

Figure 9. Same as Figure 8 but with signal tracked in closed-loop mode with fly wheeling enabled (model B). Values of $z_{50\%}$ are 3.4, 2.3, and 1.5 km for 40, 45, and 50 dB Hz, respectively. The solid line (Figure 9, left) marks the ideal receiver ("ideal rcvr.") result (Figure 8).

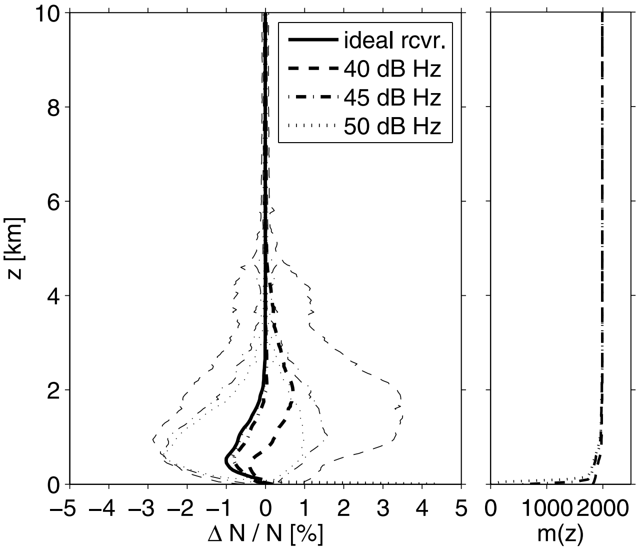

Figure 11. Same as Figure 10 but with Doppler frequency model shifted by +10 Hz. Values of $z_{50\%}$ are 0.023 and 0.086 km for 45 and 50 dB Hz.

motivated by SNR_v values typically observed in CHAMP occultation events. Figure 14 shows the normalized histogram distribution of C/A SNR_v derived from 4526 CHAMP observations collected during January 2004. While at midlatitudes and high latitudes SNR_v varies between about 200 and 900 V/V with a mean value of 576 V/V (dashed line), in the Tropics SNR_v extends from about 200 V/V (C/N_0 = 43.0 dB Hz) to about 700 V/V (C/N_0 = 53.9 dB Hz) with a mean value of 511 V/V (solid).

[43] The simulation results without signal tracking (ideal receiver) are plotted in Figure 8. In a control run we restrict the comparison to the height range above z_{CR} + 100 m and obtain a mean fractional retrieval error and standard deviation below 0.01% and 0.03%, respectively (dashed lines). Here, z_{CR} denotes the largest altitude where critical refraction is observed. As noted above, 58.3% of the refractivity profiles exhibit critical refraction; below 3 km this subset generates a negative bias of up to −1% and a standard deviation of about 2% (solid lines).

[44] All in all, the simulations are performed with five different signal tracking models:

[45] 1. Model A is the ideal receiver which exactly reproduces the signal at its input; noise contributions are not included in the simulations using model A.

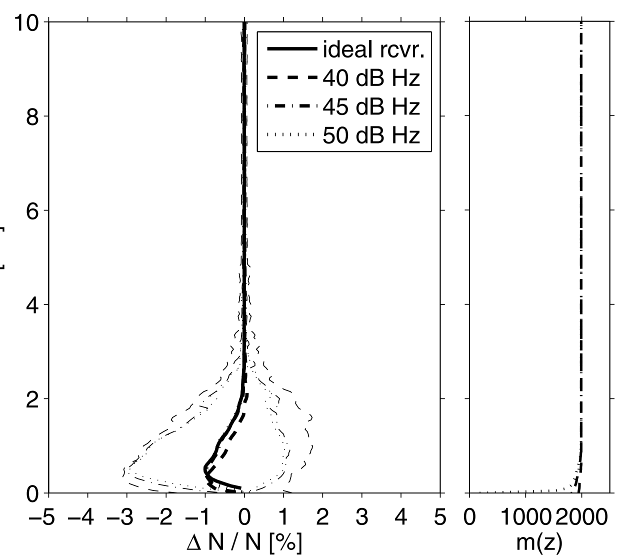

Figure 10. Same as Figure 8 but with signal tracked in open-loop mode (model C). Value of $z_{50\%}$ is 0.023 km for 50 dB Hz. At 40 and 45 dB Hz the number of retrieved data points exceeds 50% at all heights rendering $z_{50\%}$ undefined.

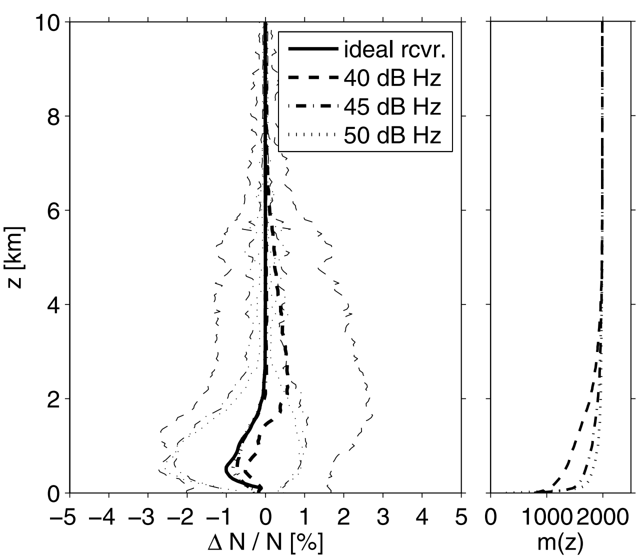

Figure 12. Same as Figure 8 but with signal tracked in closed-loop mode with carrier loop bandwidth reduced to 5 Hz (model D). Values of $z_{50\%}$ are 0.11, 0.025, and 0.039 km for 40, 45, and 50 dB Hz, respectively.

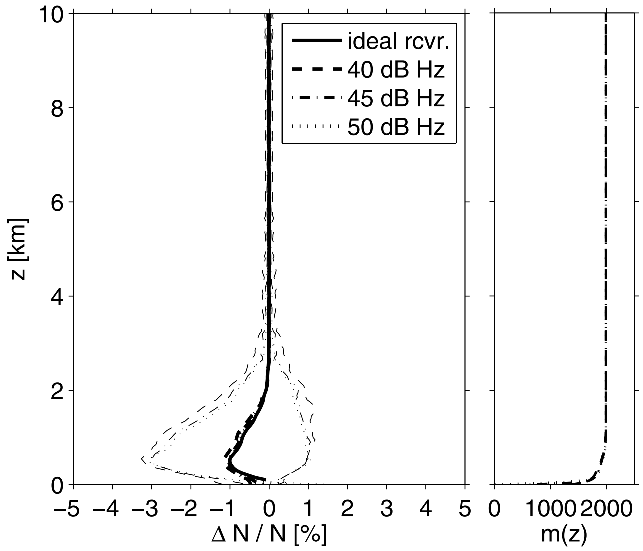

Figure 13. Same as Figure 8 but with signal tracked in closed-loop mode with second-order loop (model E). Values of $z_{50\%}$ are 0.019 and 0.040 km for 45 and 50 dB Hz, respectively.

[46] 2. The reference receiver (model B) uses closed-loop tracking, two-quadrant phase extraction with a third-order loop and 30 Hz loop bandwidth; model B is capable of fly wheeling. Qualitatively, model B corresponds to the current configuration of the BlackJack receiver aboard CHAMP.

[47] 3. Model C is the implementation of an open-loop receiver which outputs inphase and quadphase correlation sums together with the phase model. In postprocessing, the total carrier phase φ_n^{Rcv} (equation (9)) is extracted from the correlation sums taking into account the 50 Hz navigation bits (section 3.2.3).

[48] 4. Model D uses closed-loop tracking with a third-order loop, however, at reduced loop bandwidth of 5 Hz; fly wheeling is deactivated.

[49] 5. Model E is an implementation of closed-loop tracking with 30 Hz loop bandwidth, but the loop order is reduced from three to two. Model E as well as model D employ four-quadrant phase extraction (data wipe off), again fly wheeling is not active.

[50] The models' receiver parameters are summarized in Table 1.

[51] The retrieval results obtained from models B–E are presented in Figures 9–13. Figures 9 (left) to 13 (left) show mean and one-sigma standard deviation profiles obtained by linear interpolation of the individual retrieval results on a equidistant altitude grid with 50 m step size; the vertical resolution of the individual profiles is about 10–15 m. No profile selection with respect to critical refraction has been performed.

[52] The retrieval results may directly be compared to the solid line in Figure 8 (left). For that purpose the ideal receiver profile (thick solid line in Figure 8 (left)) is repeated in Figures 9–13. We note that $m(z)$ in Figure 8 (right) starts to decrease already at 2 km altitude. Below that altitude the occurrence of critical layers introduces sharp cutouts in the FSI amplitude. If these amplitude drops reach below 50% of the maximum FSI amplitude the bending angle profile is clipped already at that altitude (see section 2.2). By adding noise to the signal (receiver models B–E) the FSI amplitude gaps are washed out and drops below 50% occur less frequently. Within the PBL, therefore, $m(z)$ (shown in Figures 9, left, to 13, left) may exceed the number of data points obtained from the ideal receiver (Figure 8).

[53] The onset of a decrease in $m(z)$ already at 4–8 km altitude (Figure 9, right) shows that the fly wheeling receiver (model B) frequently loses tracking lock in the midtroposphere before reaching layers of critical refraction. Since loss of lock tends to occur at or above critical layers one would expect that the subset of successfully tracked signals minimizes the bias. However, a significant negative bias is observed below 5 km altitude. Within the PBL critical refraction might contribute to the negative N bias; above 3 km receiver-induced errors are the most likely cause, since the occurrence of critical refraction above that altitude can be excluded.

[54] The comparison between simulation results obtained by the open-loop receiver (Figure 10) and results produced by the fly wheeling receiver with two-quadrant phase extraction (Figure 9) highlights the significant negative bias and enhanced standard deviation introduced by the latter. The open-loop refractivities (dashed, dash-dotted and dotted lines in Figure 10) exhibit almost no bias and reduced standard deviation with respect to the ideal receiver (solid line).

[55] The choice of the open-loop Doppler model (equation (21)) implies that the retrieved frequency profiles f_n^{Rcv} are bias-free with respect to the true profiles. In order to address the question whether f_n^{Rcv} remains bias-free if the model is biased with respect to the truth, i.e., $\langle f_n^{\mathrm{model}} - f_n^{(j)} \rangle$

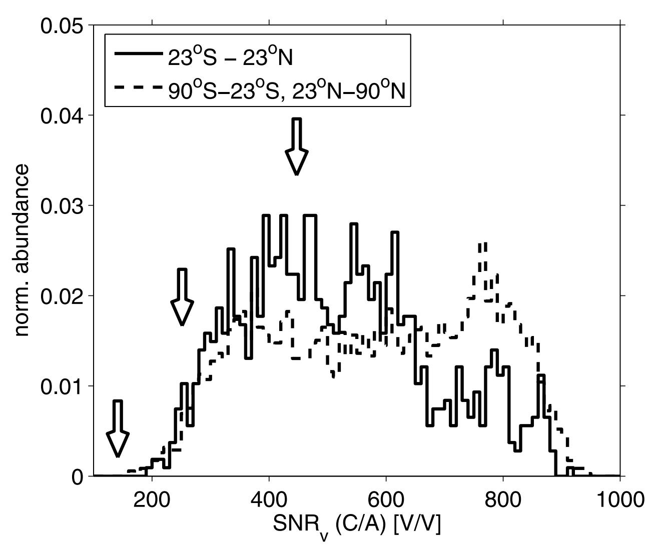

Figure 14. Normalized occurrence distribution of L1 C/A voltage signal-to-noise ratios derived from January 2004 CHAMP occultation data in the Tropics (solid line) and at mid/high latitude (dashed). Each distribution is normalized to the corresponding total number of events, which are 1073 and 3453 observations, respectively. The signal-to-noise ratios are extracted from the profiles' initial, unattenuated sections. The arrows mark the signal-to-noise density ratios of 40, 45, and 50 dB Hz.

Table 1. Characteristics of the Five Receiver Models Used in the Simulations

Receiver Model	Tracking	Loop Bandwidth	Loop Order	Phase Extraction	Comments
A	no				ideal receiver
B	closed-loop fly wheeling	30 Hz	3	two-quadrant	"CHAMP-like"
C	open-loop			four-quadrant	
D	closed-loop	5 Hz	3	four-quadrant	
E	closed-loop	30 Hz	2	four-quadrant	

$\neq$ 0, the open-loop simulation was repeated with the Doppler model f_n^{model} replaced by $f_n^{\text{model}} + \Delta f$ and Δf = +10 Hz; Figure 11 shows the result. Whereas the frequency offset has no visible effect at density ratios of 45 and 50 dB Hz, at C/N_0 = 40 dB Hz a positive bias on the order of 0.5% is observed. Clearly, these systematic deviations between retrieved and true frequencies are correlated with low signal strength. The relation between frequency bias and SNR_v is shown in Figure 15 using data from simulation run 10 (compare Figure 1). The mean deviation averaged over SNR_v bins of width 10 V/V is plotted for Δf = 0 Hz (solid line), Δf = +10 Hz (dashed) and $\Delta f = -10$ Hz (dash-dotted). For clarity the scale of vertical axis has been restricted to ±5 Hz, the individual data points (marked in grey) extend to about ±40 Hz at SNR_v < 20 V/V.

[56] The fact that a bias in the model frequency f_n^{model} introduces a corresponding bias in the retrieved frequency f_n^{Rcv} for $\text{SNR}_\text{v} \rightarrow 0$ can be understood by writing equation (9) in terms of frequencies; we obtain

$$f_n^{\text{Rcv}} = f_n^{\text{model}} + \left(\Phi_{n+1}^R - \Phi_n^R\right)/(2\pi\, T) \tag{22}$$

with $f_n^{\text{model}} = f_n^{\text{NCO}}$. For $\text{SNR}_\text{v} \rightarrow 0$ the residual phases Φ_n^R and Φ_{n+1}^R are randomly distributed between $-\pi$ and $+\pi$,

$$\langle f_n^{\text{Rcv}} \rangle = f_n^{\text{model}} + \langle \Phi_{n+1}^R - \Phi_n^R \rangle/(2\pi\, T) \rightarrow f_n^{\text{model}} \tag{23}$$

Here, angle brackets denote the ensemble mean over the simulation data set (equation (21)). If f_n^{model} is biased with respect to the true frequency, then, in the limit $\text{SNR}_\text{v} \rightarrow 0$, f_n^{Rcv} will be biased as well. We note, however, that this open-loop bias is a minor effect in the midtroposphere and lower troposphere and is relevant only for weak signals (Figure 11).

[57] In comparing the results obtained by open- and closed-loop tracking, it is instructive to illuminate the role played by the NCO phase. In the closed-loop approach the loop is designed to follow all phase accelerations within multipath regions; the residual phase adds only minor corrections to the total phase. In open-loop mode, on the other hand, the NCO phase characterizes the smooth background state and the small-scale structures induced by multipath interference patterns are captured by the residual phase. We propose a combination of both techniques: the sensitivity of the loop is degraded to achieve a better resistivity against noise-induced phase accelerations. The multipath interference patterns are then recovered to a lesser extent from the NCO phase and to a higher degree from the residual phase (see discussion of Figure 16).

[58] Two methods to reduce the loop sensitivity are investigated: first, the loop bandwidth is reduced from 30 to 5 Hz (model D), the result is plotted in Figure 12. The comparison with Figure 9 shows an improvement, both in terms of bias and standard deviation. In addition, receiver model D tracks to significantly lower altitudes with $z_{50\%}$ of 0.11, 0.025 and 0.039 km for C/N_0 = 40, 45 and 50 dB Hz, respectively. Still, at C/N_0 = 40 dB Hz the retrieved refractivities are biased by up to +0.5% and standard deviations exceed 2%.

[59] In the second approach the loop order is reduced from three to two, whereas the loop bandwidth is kept at 30 Hz. The retrieval results plotted in Figure 13 compare favorably with the open-loop results (Figure 10) with respect to bias, standard deviation and loss-of-lock altitude. Indeed, closed-loop tracking with a second-order loop seems to be less sensitive to noise-induced phase accelerations and succeeds in shifting the loss-of-lock altitude downward. The improvements gained by model E over a third-order loop, but otherwise identical receiver is exemplarily illustrated in Figure 16. It shows the NCO frequency profiles obtained from simulation run 10 (compare Figure 1) during the last 10 s of the occultation event. The second-order loop (model E) maintains lock until 90.5 s occultation time, whereas the third-order loop loses the signal already 5 s earlier. For comparison the true frequency (thin solid line) is plotted as well. Comparison with the insert in Figure 1 shows that the third-order loop's loss of lock at 85.2 s is not triggered by enhanced phase accelerations, but by low SNR_v. We note that in this simulation event the fly

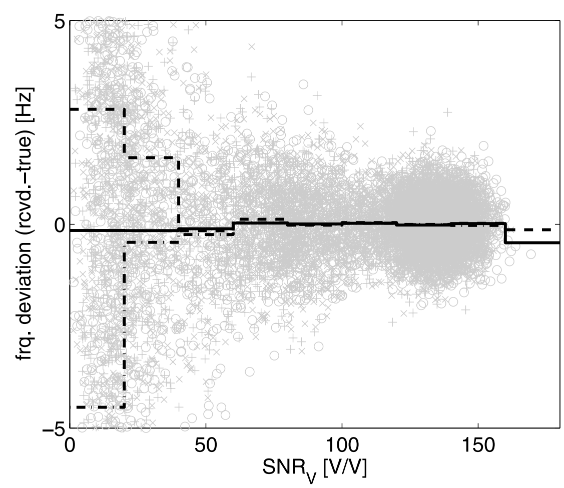

Figure 15. Deviation between retrieved and true frequency as a function of voltage signal-to-noise ratio at C/N_0 = 40 dB Hz extracted from simulation run 10 (Figure 1). The signal is tracked in open-loop mode with Doppler model shifted by +10, 0 and -10 Hz. The corresponding frequency deviations averaged over bins of width 10 V/V are plotted as dashed, solid, and dash-dotted lines, respectively; the individual data points are marked in grey.

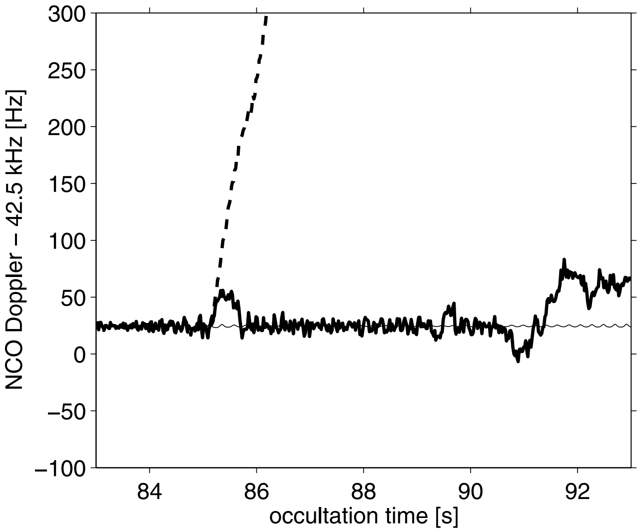

Figure 16. NCO Doppler frequency for second-order (solid) and third-order (dashed) closed-loop tracking as a function of occultation time. The second-order loop experience loss of lock at 90.5 s occultation time; the third-order loop already at 85.2 s. The thin line marks the true Doppler profile. An offset of 42.5 kHz is subtracted for clarity.

wheeling receiver (model B) ceases to track the signal already at 67.5 s occultation time.

5. Feasibility of Data Wipe Off

[60] It was noted that signal tracking using four-quadrant phase extraction requires knowledge of the 50 Hz data bit in order to demodulate the signal. Since to the best of our knowledge the GPS navigation messages are not publicly available prior to transmission the data bits have to be predicted, transmitted by the receiver and compared to the true data bits (monitored by an appropriate ground station network) during postprocessing. We briefly discuss the feasibility of this approach.

[61] The GPS navigation message is organized in frames of 1500 bit transmitted during 30 s. Each frame consists of five 300 bit subframes [*Kaplan*, 1996; *Misra and Enge*, 2002]. Subframes 1 to 3 repeat every 30 s, subframes 4 and 5 change 25 times increasing the repetition interval to 12.5 min. Demodulation is performed with predicted navigation data bits $D_n^{(p)}$. A receiver capable of data wipe off outputs $D_n^{(p)}$ in addition to phase and amplitude data. During postprocessing of the data $D_n^{(p)}$ is compared to the true data bits D_n and those occultation events recorded with a wrong prediction are flagged and removed from data set.

[62] In order to obtain an estimate on the predictability of D_n, one week of GPS data collected by a modified GPS receiver at GeoForschungsZentrum Potsdam (52.38°N, 13.07°E) was analyzed. From 13 June to 19 June 2004 (GPS week number 1275) the instrument recorded the navigation messages of all 28 active GPS satellites, in total 676,873 subframes. Our prediction algorithm assumes that the 53 different types of subframes (subframes 1–3 and 25 versions of subframe 4 and 5) remain constant with a repeat cycle of 12.5 min except for the time information (time-of-week count message) [*Kaplan*, 1996; *Misra and Enge*, 2002]. The predicted time tag in the second word of each subframe is obtained by incrementing the time-of-week count message. Despite the algorithmic simplicity 664,717 subframes are predicted correctly, only 12,156 out of 676,873 (less than 2%) predictions fail.

6. Conclusions

[63] An analysis of 1992 radiosonde soundings over the Atlantic Ocean between 45°S and 45°N shows that critical refraction in the marine environment is restricted to altitudes below 3 km. Within the PBL more than 50% of the observations show vertical refractivity gradients below the value of $-157\ \mathrm{km}^{-1}$.

[64] CHAMP refractivities observed within the same geographical region exhibit a negative bias with respect to ECMWF at altitudes of up to 5 km. The bias below 3 km may contain contributions from critical refraction; in most occultation events, however, the fly wheeling receiver loses lock at or above the critical refraction layer. The qualitative agreement between the simulated and observed results suggests that the CHAMP bias above 3 km is related to fly wheeling and two-quadrant phase extraction. Receivers using open-loop tracking or closed-loop tracking with a reduced loop order yield improvements in the midtroposphere and lower troposphere at altitude below 6–8 km in terms of retrieval bias, standard deviation and loss-of-lock altitude. At low signal-to-noise ratios of 141 V/V (C/N_0 = 40 dB Hz) our open-loop tracking results are biased toward the Doppler frequency model. Though, this bias should not be regarded as a serious limitation of future open-loop receivers, since their specifications call for significantly larger C/N_0 values.

[65] The simulation results show that open-loop tracking as well as closed-loop tracking with reduced loop order yield significantly smaller biases and standard deviations of the fractional refractivity errors compared to fly wheeling enabled receivers. Thus we consider second-order closed-loop tracking a viable alternative to open loop. Regardless of which option is selected in future receivers we expect the most significant bias reduction in the midtroposphere at altitudes between 3 and 5 km. Below 3 km a large fraction of the observations at low latitudes are affected by critical refraction layers causing current RO receivers to lose tracking lock too early. Since the occurrence of critical refraction introduces negative biases as well, provided signal tracking lock is maintained down to the ground, the expected bias reduction due to improved tracking techniques may partly be outweighed by the lowering of the loss-of-lock altitude. Furthermore, throughout the lower and midtroposphere the standard deviation of the fractional refractivity error is estimated to be significantly smaller compared to current CHAMP observations.

[66] **Acknowledgments.** We thank H.-H. Benzon, J. Christensen, A. von Engeln, M. E. Gorbunov, A. S. Jensen, T. Meehan, R. Neuber, and S. Sokolovskiy for helpful suggestions and fruitful discussions. Comments by anonymous reviewers on several versions of this paper are gratefully acknowledged. Their corrections, suggestions and remarks considerably improved the quality of this study. The European Centre for Medium-Range Weather Forecasts provided meteorological analysis fields. Part of this work

was performed when the first author was GRAS SAF visiting scientist at the Danish Meteorological Institute, Copenhagen, Denmark.

References

Ao, C. O., T. K. Meehan, G. A. Hajj, A. J. Mannucci, and G. Beyerle (2003), Lower-troposphere refractivity bias in GPS occultation retrievals, *J. Geophys. Res.*, *108*(D18), 4577, doi:10.1029/2002JD003216.

Ashby, N. (2003), Relativity in the Global Positioning System, *Living Rev. Relativity*, *6*(1) [online]. (Available at http://www.livingreviews.org/lrr-2003-1)

Bevis, M., S. Businger, S. Chiswell, T. A. Herring, R. A. Anthes, C. Rocken, and R. H. Ware (1994), GPS meteorology: Mapping zenith wet delays onto precipitable water, *J. Appl. Meteorol.*, *33*(3), 379–386.

Beyerle, G., M. E. Gorbunov, and C. O. Ao (2003), Simulation studies of GPS radio occultation measurements, *Radio Sci.*, *38*(5), 1084, doi:10.1029/2002RS002800.

Fjeldbo, G., A. J. Kliore, and V. R. Eshleman (1971), The neutral atmosphere of Venus as studied with the Mariner V radio occultation experiments, *Astron. J.*, *76*(2), 123–140.

Gorbunov, M. E. (2002), Radio-holographic analysis of Microlab-1 radio occultation data in the lower troposphere, *J. Geophys. Res.*, *107*(D12), 4156, doi:10.1029/2001JD000889.

Gorbunov, M. E. (2003), An asymptotic method of modeling radio occultations, *J. Atmos. Sol. Terr. Phys.*, *65*, 1361–1367, doi:10.1016/j.jastp.2003.09.001.

Gorbunov, M. E., and K. B. Lauritsen (2004), Analysis of wave fields by Fourier integral operators and their application for radio occultations, *Radio Sci.*, *39*, RS4010, doi:10.1029/2003RS002971.

Gorbunov, M. E., S. V. Sokolovsky, and L. Bengtsson (1996), Space refractivity tomography of the atmosphere: Modeling of direct and inverse problems, *Rep. 210*, Max-Planck-Inst. für Meteorol., Hamburg, Germany.

Hajj, G. A., E. R. Kursinski, L. J. Romans, W. I. Bertiger, and S. S. Leroy (2002), A technical description of atmospheric sounding by GPS occultation, *J. Atmos. Sol. Terr. Phys.*, *64*(4), 451–469.

Hajj, G. A., et al. (2004), CHAMP and SAC-C atmospheric occultation results and intercomparisons, *J. Geophys. Res.*, *109*, D06109, doi:10.1029/2003JD003909.

Healy, S. (2001), Radio occultation bending angle and impact parameter errors caused by horizontal refractive index gradients in the troposphere: A simulation study, *J. Geophys. Res.*, *106*(D11), 11,875–11,890.

Heise, S., J. Wickert, G. Beyerle, T. Schmidt, and C. Reigber (2006), Global monitoring of tropospheric water vapor with GPS radio occultation aboard CHAMP, *Adv. Space Res.*, doi:10.1016/j.asr.2005.06.066, in press.

Jensen, A. S., M. S. Lohmann, H.-H. Benzon, and A. S. Nielsen (2003), Full spectrum inversion of radio occultation signals, *Radio Sci.*, *38*(3), 1040, doi:10.1029/2002RS002763.

Kaplan, E. D. (1996), *Understanding GPS: Principles and Applications*, Artech House, Norwood, Mass.

Kuo, Y.-H., T.-K. Wee, S. Sokolovskiy, C. Rocken, W. Schreiner, D. Hunt, and R. A. Anthes (2004), Inversion and error estimation of GPS radio occultation data, *J. Meteorol. Soc. Jpn.*, *82*(1B), 507–531.

Kursinski, E., and G. Hajj (2001), A comparison of water vapor derived from GPS occultations and global weather analyses, *J. Geophys. Res.*, *106*(D1), 1113–1138.

Kursinski, E. R., G. A. Hajj, J. T. Schofield, R. P. Linfield, and K. R. Hardy (1997), Observing Earth's atmosphere with radio occultation measurements using Global Positioning System, *J. Geophys. Res.*, *102*(D19), 23,429–23,465.

Kursinski, E. R., G. A. Hajj, S. S. Leroy, and B. Herman (2000), The GPS radio occultation technique, *Terr. Atmos. Oceanic Sci.*, *11*(1), 53–114.

Leiterer, U., H. Dier, and T. Naebert (1997), Improvements in radiosonde humidity profiles using RS80/RS90 radiosondes of Vaisala, *Beitr. Phys. Atmos.*, *70*(4), 319–336.

Marquardt, C., K. Labitzke, C. Reigber, T. Schmidt, and J. Wickert (2001), An assessment of the quality of GPS/MET radio limb soundings during February 1997, *Phys. Chem. Earth, Part A*, *26*(3), 125–130.

Marquardt, C., K. Schöllhammer, G. Beyerle, T. Schmidt, J. Wickert, and C. Reigber (2003), Validation and data quality of CHAMP radio occultation data, in *First CHAMP Mission Results for Gravity, Magnetic and Atmospheric Studies*, edited by C. Reigber, H. Lühr, and P. Schwintzer, pp. 384–396, Springer, New York.

Melbourne, W. G., E. S. Davis, C. B. Duncan, G. A. Hajj, K. R. Hardy, E. R. Kursinski, T. K. Meehan, L. E. Young, and T. P. Yunck (1994), The application of spaceborne GPS to atmospheric limb sounding and global change monitoring, *JPL Publ., 94-18*.

Misra, P., and P. Enge (2002), Global positioning system: Signals, measurements, and performance, report, Navtech Seminars and GPS Supply, Alexandria, Va.

Reigber, C., H. Lühr, and P. Schwintzer (2002), CHAMP mission status, *Adv. Space Res.*, *30*(2), 129–134.

Reigber, C., H. Lühr, P. Schwintzer, and J. Wickert (2005), *Earth Observation With CHAMP: Results From Three Years in Orbit*, Springer, New York.

Rocken, C., et al. (1997), Analysis and validation of GPS/MET data in the neutral atmosphere, *J. Geophys. Res.*, *102*(D25), 29,849–29,866.

Sokolovskiy, S. (2004), Open loop tracking and inverting GPS radio occultation signals: Simulation study, in *Occultations for Probing Atmosphere and Climate*, edited by G. Kirchengast, U. Foelsche, and A. K. Steiner, pp. 39–51, Springer, New York.

Sokolovskiy, S. V. (2001), Tracking tropospheric radio occultation signals from low Earth orbit, *Radio Sci.*, *36*(3), 483–498.

Sokolovskiy, S. V. (2003), Effect of superrefraction on inversions of radio occultation signals in the lower troposphere, *Radio Sci.*, *38*(3), 1058, doi:10.1029/2002RS002728.

Sokolovskiy, S., C. Rocken, D. Hunt, W. Schreiner, J. Johnson, D. Masters, and S. Esterhuizen (2005), Inversion of open-loop radio occultation signals at CDAAC, paper presented at Second GPS Radio Occultation Data Users Workshop, National Conference Center, Lansdowne, Va.

Stephens, S. A., and J. B. Thomas (1995), Controlled-root formulation for digital phase-locked loops, *IEEE Trans. Aerospace Electron. Syst.*, *31*(1), 78–95.

Syndergaard, S. (2000), On the ionosphere calibration in GPS radio occultation measurements, *Radio Sci.*, *35*(3), 865–884.

Thomas, J. B. (1989), An analysis of digital phase-locked loops, *JPL Publ., 89-2*.

Tsui, J. B.-Y. (2000), *Fundamentals of Global Positioning System Receivers: A Software Approach*, 258 pp., John Wiley, Hoboken, N. J.

Vaisala (1989), Upper air systems: RS80 radiosondes, technical report, Vaisala GmbH, Hamburg, Germany.

von Engeln, A., G. Nedoluha, and J. Teixeira (2003), An analysis of the frequency and distribution of ducting events in simulated radio occultation measurements based on ECMWF fields, *J. Geophys. Res.*, *108*(D21), 4669, doi:10.1029/2002JD003170.

Wickert, J., et al. (2001), Atmosphere sounding by GPS radio occultation: First results from CHAMP, *Geophys. Res. Lett.*, *28*(17), 3263–3266.

Wickert, J., T. Schmidt, G. Beyerle, R. König, C. Reigber, and N. Jakowski (2004), The radio occultation experiment aboard CHAMP: Operational data analysis and validation of atmospheric profiles, *J. Meteorol. Soc. Jpn.*, *82*(1B), 381–395.

Yunck, T. P., C.-H. Liu, and R. Ware (2000), A history of GPS sounding, *Terr. Atmos. Oceanic Sci.*, *11*(1), 1–20.

G. Beyerle, S. Heise, M. Rothacher, T. Schmidt, and J. Wickert, GeoForschungsZentrum Potsdam (GFZ), Department 1, Geodesy and Remote Sensing, Telegrafenberg, D-14473 Potsdam, Germany. (gbeyerle@gfz-potsdam.de; stefan.heise@gfz-potsdam.de; rothacher@gfz-potsdam.de; tschmidt@gfz-potsdam.de; jens.wickert@gfz-potsdam.de)

G. König-Langlo, Alfred Wegener Institute for Polar and Marine Research, Postfach 12 0161, D-27515 Bremerhaven, Germany. (gkoenig@awi-bremerhaven.de)

K. B. Lauritsen, Danish Meteorological Institute, Lyngbyvej 100, DK-2100 Copenhagen, Denmark. (kbl@dmi.dk)